# Hybrid Iodide Perovskites of Divalent Alkaline Earth and Lanthanide Elements

Greggory T. Kent[a], Jiale Zhuang[a], Kaitlin R. Albanese[a][b], Arava Zohar[a], Emily Morgan[a], Anna Kallistova[a], Linus Kautzsch[a], Alexander A. Mikhailovsky[b], Pratap Vishnoi[c], Ram Seshadri*[a][b] and Anthony K. Cheetham*[a][d]

[a] Materials Department and Materials Research Laboratory, University of California, Santa Barbara, CA 93106 United States

[b] Department of Chemistry and Biochemistry, University of California, Santa Barbara, CA 93106, United States

[c] New Chemistry Unit and International Centre for Materials Science, Jawaharlal Nehru Centre for Advanced Scientific Research, Bangalore 560064, India

[d] Department of Materials Science & Engineering, National University of Singapore, 117576, Singapore

*Supporting Information Placeholder*

**ABSTRACT:** Hybrid halide perovskites $AM^{II}X_3$ ($A$ = ammonium cation, $M^{II}$ = divalent cation, $X$ = Cl, Br, I) have been extensively studied, but have only previously been reported for the divalent carbon group elements Ge, Sn and Pb. While they have displayed an impressive range of optoelectronic properties, the instability of $Ge^{II}$ and $Sn^{II}$ and the toxicity of Pb have stimulated significant interest in finding alternatives to these carbon group–based perovskites. Here we describe the low temperature solid-state synthesis of five new hybrid iodide perovskites centered around divalent alkaline earth and lanthanide elements, with the general formula $AM^{II}I_3$ ($A$ = methylammonium, MA; $M^{II}$ = Sr, Sm, Eu, and $A$ = formamidinium, FA; $M^{II}$ = Sr, Eu). Structural, calorimetric, optical, photoluminescence, and magnetic properties of these materials are reported.

## Introduction

The last 15 years of halide perovskite [$AM^{II}X_3$] research has seen an explosion of interest, principally related to the potential of these materials in optoelectronic and photovoltaic (PV) devices.[1,2] By tuning the overall stoichiometry and $M$-site oxidation state, these perovskite structures can adopt dimensions that range from 3D to 0D.[3–5] Consequently, vast libraries of new structures and compositions with exciting properties have been generated. While lower dimensional structures (i.e. 2D to 0D) have shown novel optical, photoluminescence, and magnetic properties, their use in PV active layers will likely always be overshadowed by the superior conductivity and performance of their 3D analogs.[4,6] Compared to their all-inorganic iodide derivatives, 3D hybrid perovskite iodide compounds have several advantages because of their lower temperature synthesis, lower cost, and the $A$-cation's large size. The best-studied 3D-hybrid iodide systems are MAPbI$_3$ (methylammonium, MA = CH$_3$NH$_3^+$) and FAPbI$_3$ (formamidinium, FA = HC(NH$_2$)$_2^+$) as well as their tin derivatives.[1,7–9] Furthermore, all of the 3D-hybrid perovskites reported to date possess carbon group elements in the $M^{II}$ site, specifically Ge, Sn, and Pb. By comparison, there are several 3D-all-inorganic iodide compositions that do not use Pb(II) or Sn(II), many with Cs or Rb in the $A$ site.[10–15] These compositions exclusively use either divalent lanthanide or alkaline earth metals in the $M^{II}$ site.

In an effort to identify possible hybrid compositions which could host non-carbon group elements, we have used a combination of the Goldschmidt Tolerance Factor (*TF*, eq S1) and the radius ratio ($\mu$, eq S2).[16] The Goldschmidt Tolerance Factor has been widely used to predict whether a perovskite composition can form (0.8 < TF < 1.0), and if it will likely form an ideal cubic structure (0.9 < TF < 1.0).[17–20] The radius ratio has been used to determine if the $M$-site metal can support an octahedron of $X^-$ anions ($X^-$ = F$^-$, Cl$^-$, Br$^-$, I$^-$). The combination of these two criteria has been used to predict large numbers of both hybrid and inorganic single and double perovskites.[19,21] For instance, we utilized both criteria to predict possible iodide double perovskites,[21] which have since been realized by both ourselves[22], and by Gamelin and coworkers.[23] *TF* and radius ratio calculations suggest the possible existence of several new 3D-hybrid perovskite iodides by using divalent lanthanide and alkaline earth metal ions in the $M^{II}$ site (Figure 1, Table S1). Among the alkaline earth metals, Sr(II) and Ca(II) closely resemble Pb(II) and Sn(II), respectively, in their ionic radii.[24,25] In addition, the ionic radii of Eu(II) and Sm(II) are similar to Pb(II),[24] while Yb(II) is close to Sn(II),[25] noting that each of these three lanthanides have reasonably accessible divalent oxidation states. The calculated *TF* and $\mu$ values for various compositions using FA or MA suggest that

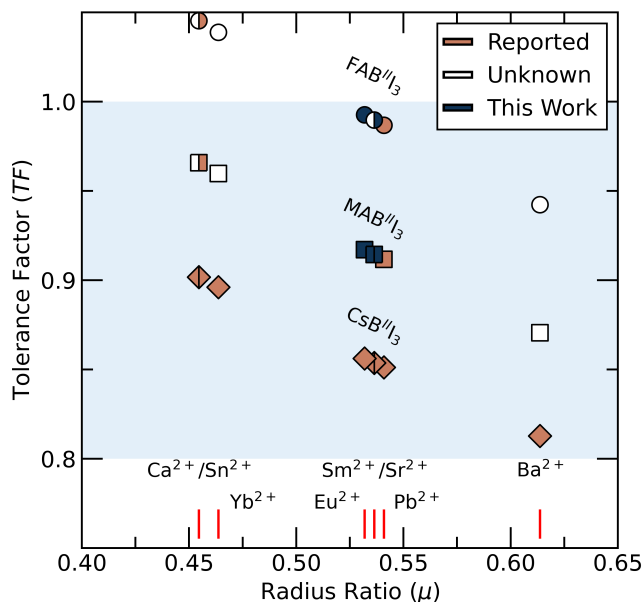many of the alkaline earth metals and lanthanides could form stable perovskite phases (Figure 1).



**Figure 1.** *TF* **vs radius ratio of known, unknown, and new compositions reported in this work with selected divalent elements. The blue region denotes the optimal *TF* range for 3D perovskite phase formation. Circles (○) denote compositions with FA$^+$, squares (□) denote compositions with MA$^+$, and diamonds (◇) denote compositions with Cs$^+$.**

Although there are no reports of hybrid perovskite iodides, $AM^{II}I_3$, beyond compositions with Ge, Sn or Pb, Mitzi and Liang discovered a 2D hybrid perovskite iodide of Eu$^{II}$ when they utilized a low temperature solid-state method to synthesize $(C_4H_9NH_3)_2EuI_4$.[26] We note that Mitzi and Liang did mention that they were able to generate MAEuI$_3$; however, their results on this composition were never published. Xiao and coworkers' attempt to generate a higher dimensional Eu(II) iodide perovskite via solution synthesis instead resulted in the formation of the 0D phase BA$_{10}$EuI$_{12}$ (BA = C$_4$H$_9$NH$_4^+$), where the EuI$_6^{4-}$ octahedra are isolated from one another.[27] In the present work, we set out to synthesize several of our predicted hybrid $AM^{II}I_3$ compounds by using a similar low temperature solid state synthetic protocol to that of Mitzi and Liang.[26] We report the synthesis and characterization of five new 3D hybrid perovskites iodides, $AM^{II}I_3$ ($A$ = MA, $M^{II}$ = Sr, Sm, Eu; $A$ = FA, $M^{II}$ = Sr, Eu). Their structures and phase transitions have been studied through Rietveld refinement and differential scanning calorimetry. Optical absorption, magnetic properties, variable temperature photoluminescence, and lifetime measurements are also detailed and compared with their relevant analogs.

### Results and Discussion

#### Synthesis and Characterization

The compounds were synthesized via solid-state reaction between the appropriate alkylammonium iodide and metal diiodide in equimolar ratios at 205 °C in an alumina crucible, under strictly air-free and anhydrous conditions (See Supporting Information). We found that where the $A$ cation was methylammonium the reaction only required 24 h to complete, whereas when formamidinium iodide was used as the $A$ cation source the reaction was slower and required 72 h for complete conversion. We were unable to synthesize FASmI$_3$, which was likely a result of a redox reaction between formamidinium and the highly reducing Sm(II). All the compounds are extremely air sensitive and decompose rapidly when exposed to air. Unlike the lead analogues, which are black and semiconducting, the Sr, Sm and Eu compounds are white, dark-green and yellow, respectively, reflecting their wider band gaps, but bearing in mind the 4f→5d transitions of Eu(II) and Sm(II).
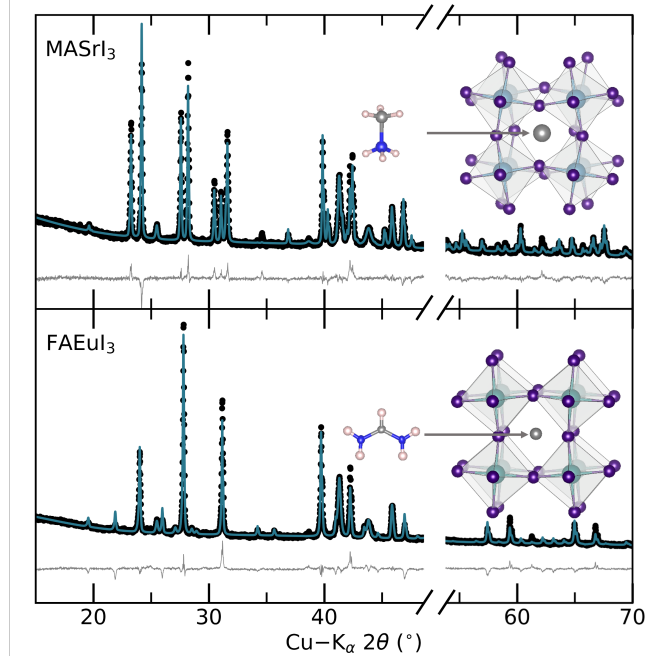


**Figure 2. PXRD of MASrI$_3$ (top), and FAEuI$_3$ (bottom) with Rietveld refinement (green line), difference (grey line), and respective structures, drawn to scale. For conciseness, the region containing the major Be reflections around 50° 2theta have been excluded.**

The structures of $AM^{II}I_3$ ($A$ = MA, $M^{II}$ = Sr, Sm, Eu; $A$ = FA, $M^{II}$ = Sr, Eu) were determined through Rietveld analysis of their laboratory XRD patterns (Figures 2 and S1). For all phases the $A$-cation has been modeled and refined as a pseudo-atom with equivalent scattering power, as previously described by Fabini and coworkers.[28] Each of the MA$M^{II}I_3$ ($M^{II}$ = Sr, Sm, Eu) compositions crystallizes in the tetragonal space group $I4/mcm$ at room temperature, where their lattice parameters and cell volumes decrease with decreasing ionic radius (Figure 2; Tables 1 and S2). The $M^{II}$–I bond distances for each compound are summarized in Table 1, and are

2

consistent with comparable $M^{II}$ ($M^{II}$ = Sr, Sm, Eu) to iodide octahedra bond distances.[10,12] At room temperature, MAPbI$_3$ also crystallizes in the same tetragonal space group, $I4/mcm$, and is isostructural to MA$M^{II}$I$_3$ ($M^{II}$ = Sr, Sm, Eu). Despite Pb(II) having a slightly larger Shannon ionic radius than Eu(II) or Sr(II), the lattice parameters and volume of MAPbI$_3$ are slightly smaller than these compositions, (Table 1);[29] this trend is also reflected in the calorimetric behavior (See calorimetry data below). The deviation from the expected trend of ionic radii arises because the Shannon radii are less reliable for iodides due to covalency effects.[30] The structures of FA$M^{II}$I$_3$ ($M^{II}$ = Sr, Eu) were also determined through Rietveld analysis of their laboratory powder XRD patterns. At room temperature, both compositions adopt the tetragonal $P4/mbm$ space group and are isostructural to β-FAPbI$_3$ (Figure 2). Similar to the methylammonium analogs, the tetragonal lattice parameters of FASrI$_3$ are slightly larger than that of FAEuI$_3$ (Table 1, Table S1). A direct comparison between the lattice parameters of FA$M^{II}$I$_3$ ($M^{II}$ = Sr, Eu) and β-FAPbI$_3$ is not feasible because at room temperature FAPbI$_3$ crystallizes in the cubic α-phase, highlighting the smaller effective size of Pb(II) in FAPbI$_3$.[28,31]

**Table 1. Lattice parameters and $M^{II}$–I bond lengths of $AM^{II}$I$_3$ compounds at $T$ = 300 K.**

| Compound | Space group | Cell parameters (Å) | $M^{II}$–I distances (Å) |
|---|---|---|---|
| MASrI$_3$ | I4/mcm | a = 8.9449(3) | 4×3.2322(1), |
| | | c = 12.9288(3) | 2×3.216(2) |
| MASmI$_3$ | I4/mcm | a = 8.9372(5) | 4×3.2262(3), |
| | | c = 12.9046(8) | 2×3.215(3) |
| MAEuI$_3$ | I4/mcm | a = 8.9191(2) | 4×3.2177(2), |
| | | c = 12.8709(4) | 2×3. 206(2) |
| FASrI$_3$ | P4/mbm | a = 9.1018(5) | 4×3.2182(2), |
| | | c = 6.4365(3) | 2×3.248(7) |
| FAEuI$_3$ | P4/mbm | a = 9.0716(2) | 4×3.2073(1), |
| | | c = 6.4146(2) | 2×3.233(5) |

Differential scanning calorimetry (DSC) carried out on the five new compounds supports the ionic radii trends observed in the XRD analysis. In the case of MA-$M^{II}$I$_3$ ($M^{II}$ = Sr, Sm, Eu) two reversible thermal transitions, one at lower temperatures, between 214 K and 228 K, and one at higher temperatures, between 415 K and 431 K are tentatively assignable to the $Pnma\leftrightarrow I4/mcm$ and the $I4/mcm\leftrightarrow Pm\overline{3}m$ phase transitions, respectively (Figures 3 and S7). These two transitions are similar to those seen in DSC experiments of MAPbI$_3$ and are separated by a similar temperature range.[8,32] However, the respective transitions for MAPbI$_3$ occur at 170 K ($Pnma\leftrightarrow I4/mcm$) and 330 K ($I4/mcm\leftrightarrow Pm\overline{3}m$), which are significantly lower temperatures than what we observed for MA$M^{II}$I$_3$ ($M^{II}$ = Eu, Sm, Sr). This is consistent

with the smaller lattice parameters of MAPbI$_3$.[29] The difference between the enthalpy change between the low and high temperature transitions can be understood by comparison with the analogous MAPbI$_3$ compound. Heating MAPbI$_3$ through the $Pnma\rightarrow I4/mcm$ transition is accompanied by an order→disorder transition of the MA$^+$ cation, whereas the high temperature $I4/mcm\leftrightarrow Pm\overline{3}m$ transition is of the disorder→disorder type.[32]
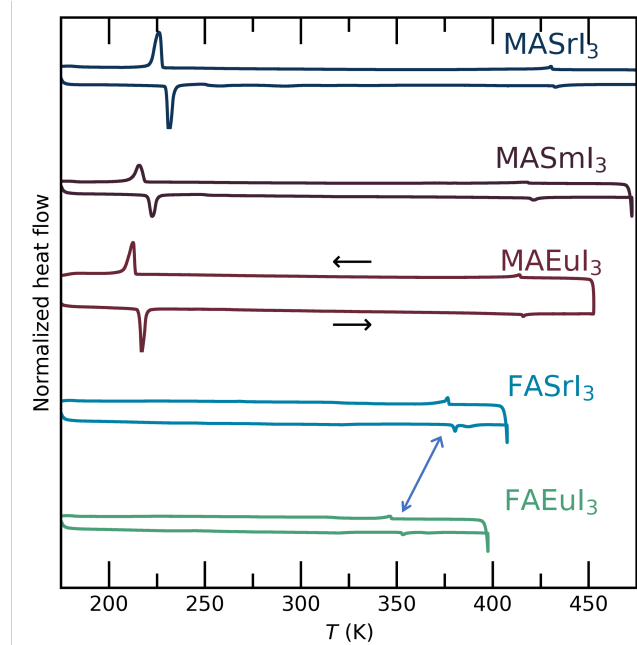


**Figure 3. DSC thermograms of $AM^{II}$I$_3$ (A = MA, $M^{II}$ = Sr, Sm, Eu; $A$ = FA, $M^{II}$ = Sr, Eu). The second heat and cool, with a ramp rate of 10 K min$^{-1}$ and exotherm up are shown. The black arrows denote the directions of the temperature ramps, while the blue arrows denote the likely $P4/mbm\leftrightarrow Pm\overline{3}m$ transition features in FA$M^{II}$I$_3$ ($M^{II}$ = Eu, Sr).**

DSC experiments carried out on FA$M^{II}$I$_3$ ($M^{II}$ = Eu, Sr) do not reveal any transitions on cooling from room temperature to 173 K (Figures 3 and S7). A reversible transition was observed to occur at higher temperatures, at 349 K and 378 K for FAEuI$_3$ and FASrI$_3$, respectively. Upon heating two endotherms within 15 K of each other are present, while only one broader exotherm can be seen on cooling. These features are reversible and are tentatively assigned to the same $P4/mbm\leftrightarrow Pm\overline{3}m$ phase transition seen in FAPbI$_3$ at 275 K.[28,31]

IR spectroscopy was used to confirm the presence of the methylammonium and formamidinium cations in their respective $AM^{II}$I$_3$ compounds. The IR spectra of MA$M^{II}$I$_3$ ($M^{II}$ = Sr, Sm, Eu) are qualitatively the same with slight changes in intensities and shifts, and are very similar to the previously reported spectrum of MAPbI$_3$ (Figure S2).[33] Similarly, the IR spectra of FA$M^{II}$I$_3$ ($M^{II}$ = Sr, Eu) are also qualitatively the same and match well to the reported IR spectrum of α-FAPbI$_3$ (Figure S3).[34] X-

3

ray photoelectron spectroscopy (XPS) spectra were obtained to examine the elemental composition and the oxidation states of metal ions. The Eu(II) 3d spectra of $A$EuI$_3$ ($A$ = MA, FA) show that the majority of the Eu is in the divalent state (Figure S4-S6).[27,35] A small amount of Eu(III) can be observed in the XPS spectrum of $A$EuI$_3$ at energies approximately 10 eV higher in energy (Figure S6 and Table S5), which could be either due to back scattering or surface oxidation.[27] In the case of MASmI$_3$, the 3d states appear at the binding energies of 1109.3 eV and 1082.6 eV (Figure S6 and Table S5), which are close to the reported value for Sm(III).[35] however, the presence of Sm(III) on the surface would be expected given the even higher air sensitivity and oxidizable nature of MASmI$_3$ compared to $A$EuI$_3$.

**Optical Absorption and Emission Properties**

We recorded the solid-state optical absorption spectra of $A$EuI$_3$ ($A$ = MA, FA) and MASmI$_3$ (Figure 4). The spectrum of MASmI$_3$ contains many features, which are primarily 4f → 5d transitions and are characteristic of Sm(II).[36-39] The optical absorption spectra of $A$EuI$_3$ ($A$ = MA, FA) both show strong absorptions centered around 370 nm that are assignable to a $4f^7$ → $4f^65d^1(t_{2g})$ transition.[40,41] The 4f → 5d transitions observed in many lanthanides (i.e. Ce(III), Sm(II), Eu(II), etc) are known to exhibit luminescence during relaxation back to their respective 4f states.[40-43] Accordingly, upon excitation at 367 nm both MAEuI$_3$ and FAEuI$_3$ exhibit luminescence centered at approximately 447 nm. The emission seen in FAEuI$_3$ was also qualitatively more intense compared to MAEuI$_3$, likely a consequence of the longer Eu–Eu distances. The emission spectra of $A$EuI$_3$ are also similar to other Eu(II) iodide species, including $A$EuI$_3$ ($A$ = Cs, Rb) and $A$Eu$_2$I$_5$ ($A$ = Cs, Rb, K).[44-46] While monitoring their respective $\lambda_{em}$ maxima, we also recorded the excitation profiles for both MAEuI$_3$ and FAEuI$_3$. In both samples the excitation spectrum contains multiple features and a maximum centered around 367 nm. The 367 nm feature is noticeably more pronounced in FAEuI$_3$ compared to the MAEuI$_3$, whose excitation spectrum shows more pronounced shoulder features. We have also performed several preliminary experiments on doping Eu(II) into MASr$_{1-x}$Eu$_x$I$_3$ (x = 0.01, 0.03, 0.05) and found a significant enhancement of the relative photoluminescent intensity at these lower dopant concentrations as well as a subtle blue shift of the peak maxima (Figure S12).

The emission spectra of MASmI$_3$ were recorded between $T$ = 77 K and 300 K (Figures 4c and S8). Excitation of MASmI$_3$ at 375 nm and 300 K shows one broad feature centered at 820 nm which is assignable to the $4f^65d^1(t_{2g})$ → $^7F_0$ transition. MASmI$_3$ shows an emission spectrum that is characteristic of Sm(II),[47] but is also slightly red-shifted compared to other reported emission spectra of Sm(II) iodide systems.[37,44] Upon cooling to 77 K the major feature blue-shifts to 811 nm and a shoulder feature, centered at approximately 833 nm, becomes

somewhat resolved. The feature at 833 nm can be assigned to the $4f^65d^1(t_{2g})$ → $^7F_1$ transition. The difference in energies between the transitions to $^7F_0$ and $^7F_1$, which corresponds to the spin-orbit coupling constant, is approximately 330 cm$^{-1}$, and agrees well with energy differences determined by others,[37,47] as well as our own magnetic data on this system (see below). Variable temperature lifetime measurements of MASmI$_3$ between $T$ = 77 K and 300 K can be fitted to a double exponential function (Figure S9). At $T$ = 77 K the two lifetimes are 628 ns and 81 ns, and upon warming to $T$ = 300 K the lifetimes decrease to 56 ns and 0.9 ns, respectively (Figure S9).
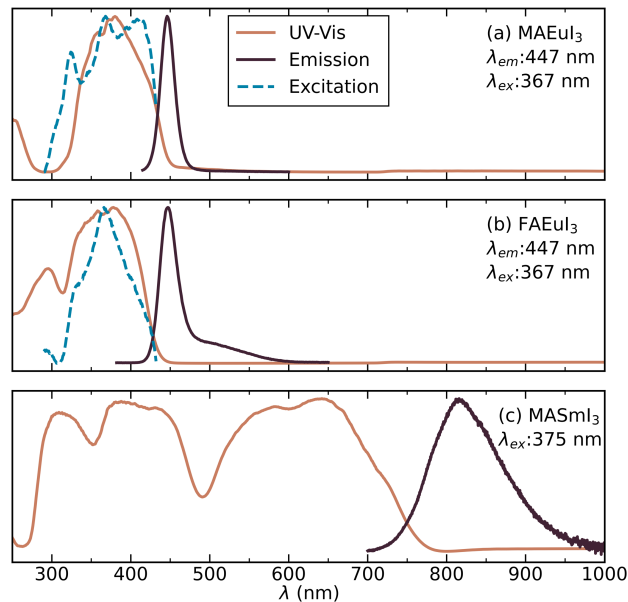


**Figure 4. Optical absorption spectra (solid orange lines) and photoluminescent excitation (dashed blue lines) and emission spectra (solid black line) of (a) MAEuI$_3$, (b) FAEuI$_3$, and (c) MASmI$_3$, collected at room temperature.**

The variable temperature photoluminescence and lifetime measurements for $A$EuI$_3$ ($A$ = MA, FA) were also recorded by excitation at 375 nm, and their respective Huang-Rhys factors ($S$),[48] phonon frequencies ($\hbar\omega$), and lifetimes ($\tau$) were obtained. The variable temperature photoluminescence of FAEuI$_3$ shows broadening and decaying intensity upon warming, as expected. A subtle blue shift in the peak maxima from 453 nm to 447 nm also occurred upon warming, and was likely a consequence of the increase in overlapping exciton-based luminescence at higher temperatures (Figure S8). The Huang-Rhys factor and phonon frequency values for FAEuI$_3$ are $S$ = 6 and $\hbar\omega$ = 151 cm$^{-1}$, respectively (Figure S10, Eq S3). These values are consistent with values of $S$ seen in other Eu(II) systems,[49,50] and the Raman vibrational frequencies seen in other lanthanide iodide systems.[22,51-53] In MAEuI$_3$, the emission intensity decreases and the peak maxima red shifts from 441 nm (77 K) to 448 nm (300 K) with increasing temperature (Figure S8). The apparent transition

4

between the *Pnma* and *I4/mcm* phases is also accompanied by a 4 nm red-shift in luminescence maxima, between 200 K and 225 K. This transition slightly affects the FWHM values at the transition; however, fitting the FWHM values to Eq S3 through the transition gives values of $S = 3$ and $\hbar\omega = 146$ cm$^{-1}$ for MAEuI$_3$ (Figure S10).

Variable temperature lifetime measurements for both FAEuI$_3$ and MAEuI$_3$ were also recorded between $T = 77$ K and 300 K (Figures S9). The lifetime curves for FAEuI$_3$ can be fitted with a single exponential function whose lifetime decreases from 605 ns at 77 K to 69 ns at 300 K (Figure S9 and S11). The lifetime curves of MAEuI$_3$ are best fitted to a double exponential function. At $T = 77$ K the two lifetimes are 928 ns and 598 ns; the faster component decreases in lifetime to 270 ns at 225 K then increases again to 382 ns at 300 K after the apparent transition from *Pnma* to *I4/mcm*. Similarly, the slow component (928 ns at 77K) remains relatively unchanged until after the respective phase transition, at which point it increases to 1134 ns at 300 K (Figure S9 and S11). This behavior has also been observed in MAPbX$_3$ thin films,[54] and is likely a consequence of the reduction in octahedral tilting and increased Eu–Eu spacing. For comparison, the lifetime of BaEu$_2$I$_5$ is around 300 ns, at 77 K, while lifetimes of Cs$M^{II}$I$_3$ ($M^{II}$ = Mg, Ca, Sr) are on the order of 700 ns at 300 K.[55,56]

**Magnetic Properties**

To further confirm the bulk oxidation states of these compounds, the magnetic susceptibilities of MASmI$_3$, MAEuI$_3$ and FAEuI$_3$ were recorded between $T = 1.8$ K and 300 K (Figure 5). As expected for a 4f$^7$ ion, both MAEuI$_3$ and FAEuI$_3$ show ideal Curie-Weiss behavior in their $1/\chi$ plots (Figure 5a and 5b).[57] Fitting these measurements to the Curie-Weiss law affords near identical room temperature magnetic moments of 8.07 $\mu_B$ per Eu(II) ion. These values agree well with the calculated spin-only moment for seven unpaired electrons (7.94 $\mu_B$).[58] The Curie-Weiss interaction parameters ($\theta$) for AEuI$_3$ ($A$ = MA, $\theta$ = –3.5 K; $A$ = FA, $\theta$ = –1.4 K) are also relatively small and becomes weaker upon moving to larger Eu–Eu distances in FAEuI$_3$ (due to the 2.53 Å radius for FA$^+$ vs 2.17 Å for MA$^+$).[17] Overall, the exchange interactions between the Eu(II) cations are very weak due to the large size of the intervening iodide ions. However, in MAEuI$_3$ a small bifurcation in the field cooled vs zero field cooled susceptibility measurements can be observed at approximately $T = 3.6$ K (Figure 5a, inset), while FAEuI$_3$ shows no deviation from linearity down to $T = 1.8$ K (Figure 5b, inset). The low temperature transition is likely due to metamagnetic behavior and is further supported by the M vs H data at 2 K (Figure S13).[59,60]
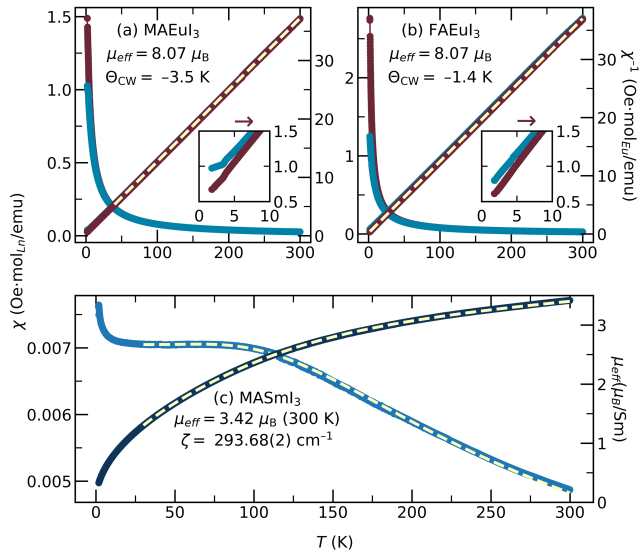


**Figure 5. Magnetic susceptibility (left y-axis), inverse magnetic susceptibility (top right y-axis), and effective magnetic moment (bottom right y-axis) plots for (a) MAEuI$_3$ (b) FAEuI$_3$, and (c) MASmI$_3$, with their respective fits (dashed lines). Insets show low temperature field cooled and zero field cooled inverse magnetic susceptibility data.**

The magnetic susceptibility of MASmI$_3$ was recorded between $T = 1.8$ K and 300 K and is shown in Figure 5c. The room temperature moment of this material is 3.42 $\mu_B$ per Sm(II) and agrees well with experimentally determined values for other Sm(II) compounds.[58] Given that Sm(II) is a 4f$^6$ ion, and isoelectronic to Eu(III), it is expected to have a $^7F_0$ ground state, and no net magnetization at low temperatures, according to the Russell-Saunders coupling scheme.[58,37,61] Upon cooling to $T = 1.8$ K, the moment decreases to 0.33 $\mu_B$ per Sm(II) as the six excited $J$ states ($^7F_6$-$^7F_1$) are thermally depopulated. Fitting the susceptibility data to a modified Van Vleck equation (Eq S5) affords a spin-orbit coupling (SOC) constant of $\zeta = 298.68(2)$ cm$^{-1}$ for MASmI$_3$ (Figure S16),[62] which agrees well with our photoluminescent data above. To the best of our knowledge, the only other example of a Sm(II) compound being fitted using variable temperature magnetic data was by Wang and coworkers, who found that SmI$_2$ in a THF solution had a SOC constant of $\zeta = 243(2)$ cm$^{-1}$.[37] Dieke and Sarup have also determined the value of $\zeta$ for Sm(II) in LaCl$_3$ and CaF$_2$ host lattices to be 272 cm$^{-1}$ and 369 cm$^{-1}$, respectively.[47] The spin-orbit coupling in Sm(II) compounds is weaker than that in the isoelectronic Eu(III) compounds, due to the higher effective nuclear charge of Eu(III) vs Sm(II). For example, the value of $\zeta$ for Eu$_2$BaZnO$_5$ (365(2) cm$^{-1}$),[61] and EuAlO$_3$ (370 cm$^{-1}$) are about 70 cm$^{-1}$ higher in energy,[63] while BaEu$_2$ZnO$_5$ (333 cm$^{-1}$) is about 35 cm$^{-1}$ higher in energy.[64] Finally, we note that the increase in the magnetic susceptibility of MASmI$_3$ below $T \approx 30$ K is likely a consequence of Van Vleck paramagnetism and a small amount of paramagnetic impurity.[65]

## Conclusions

To summarize, through rational design rules and low temperature solid-state synthesis we have obtained the first 3D-hybrid halide perovskites that do not have a carbon group elements in the $M^{II}$ site. All compositions are isostructural with their $APbI_3$ counterparts and have lattice parameters that are slightly larger, consistent with the calorimetry results. The optical properties of the Eu(II) compounds are of particular note, exhibiting photoluminescence that is reminiscent of Eu(II)-based phosphors.[66] The magnetic properties of $MASmI_3$ represent a rare-example of magnetic-moment quenching in a $f^6$ Sm(II) compound at low temperatures. Significantly, all of our new compounds are free of lone-pairs, providing opportunities to make direct comparisons to the crystal and electronic structures of compositions with lone-pair $M^{II}$ cations (i.e. Pb(II), Sn(II)).[67,68] Future studies will examine examples of other cations and anions on the $A$ and $X$ sites, respectively, and also explore the use of these synthetic methods for the creation of lower dimensional structures such as Ruddlesden-Popper or Dion Jacobson phases.

## ASSOCIATED CONTENT

The Supporting Information is available free of charge on the ACS Publications website.

Additional experimental details, crystallographic details (Table S2-S4, Figure S1), IR spectra (Figures S2 and S3), XPS spectra (Figures S4-S6, Table S5), DSC measurements (Figure S7), variable temperature photoluminescent/lifetime measurements (Figures S8-S12), and magnetic moment vs field data (Figures S13-S15) may be found in the supporting information. (PDF)

## AUTHOR INFORMATION

### Corresponding Author

**Ram Seshadri** - Materials Department and Materials Research Laboratory, University of California Santa Barbara, CA 93106, United States; ORCID: ocid.org/0000-0001-5858-4027; Email: seshadri@mrl.ucsb.edu

**Anthony K. Cheetham** - Materials Department and Materials Research Laboratory, University of California Santa Barbara, CA 93106, United States; Department of Materials Science & Engineering, National University of Singapore, 117576 Singapore; ORCID: orcid.org/0000-0003-1518-4845 Email: akc30@cam.ac.uk

### Notes
No competing financial interests have been declared.

## ACKNOWLEDGMENT

## REFERENCES

(1)    Kojima, A.; Teshima, K.; Shirai, Y.; Miyasaka, T. Organometal Halide Perovskites as Visible-Light Sensitizers for Photovoltaic Cells. *J. Am. Chem. Soc.* **2009**, *131* (17), 6050–6051. https://doi.org/10.1021/ja809598r.

(2)    Jena, A. K.; Kulkarni, A.; Miyasaka, T. Halide Perovskite Photovoltaics: Background, Status, and Future Prospects. *Chem. Rev.* **2019**, *119* (5), 3036–3103. https://doi.org/10.1021/acs.chemrev.8b00539.

(3)    Li, W.; Wang, Z.; Deschler, F.; Gao, S.; Friend, R. H.; Cheetham, A. K. Chemically Diverse and Multifunctional Hybrid Organic–Inorganic Perovskites. *Nat Rev Mater* **2017**, *2* (3), 16099. https://doi.org/10.1038/natrevmats.2016.99.

(4)    Hong, K.; Van Le, Q.; Young Kim, S.; Won Jang, H. Low-Dimensional Halide Perovskites: Review and Issues. *J. Mater. Chem. C* **2018**, *6* (9), 2189–2209. https://doi.org/10.1039/C7TC05658C.

(5)    Evans, H. A.; Mao, L.; Seshadri, R.; Cheetham, A. K. Layered Double Perovskites. *Annu. Rev. Mater. Res.* **2021**, *51* (1), 351–380. https://doi.org/10.1146/annurev-matsci-092320-102133.

(6)    Sun, S.; Lu, M.; Gao, X.; Shi, Z.; Bai, X.; Yu, W. W.; Zhang, Y. 0D Perovskites: Unique Properties, Synthesis, and Their Applications. *Adv. Sci.* **2021**, *8* (24), 2102689. https://doi.org/10.1002/advs.202102689.

(7)    Lee, M. M.; Teuscher, J.; Miyasaka, T.; Murakami, T. N.; Snaith, H. J. Efficient Hybrid Solar Cells Based on Meso-Superstructured Organometal Halide Perovskites. *Science* **2012**, *338* (6107), 643–647. https://doi.org/10.1126/science.1228604.

(8)    Stoumpos, C. C.; Malliakas, C. D.; Kanatzidis, M. G. Semiconducting Tin and Lead Iodide Perovskites with Organic Cations: Phase Transitions, High Mobilities, and Near-Infrared Photoluminescent Properties. *Inorg. Chem.* **2013**, *52* (15), 9019–9038. https://doi.org/10.1021/ic401215x.

(9)    Koh, T. M.; Fu, K.; Fang, Y.; Chen, S.; Sum, T. C.; Mathews, N.; Mhaisalkar, S. G.; Boix, P. P.; Baikie, T. Formamidinium-Containing Metal-Halide: An Alternative Material for Near-IR Absorption Perovskite Solar Cells. *J. Phys. Chem. C* **2014**, *118* (30), 16458–16462. https://doi.org/10.1021/jp411112k.

(10)    Schilling, G.; Meyer, G. Ternäre Bromide und Iodide zweiwertiger Lanthanide und ihre Erdalkali-Analoga vom Typ $AMX_3$ und $AM_2X_5$. *Z. Anorg. Allg. Chem* **1996**, *622* (5), 759–765. https://doi.org/10.1002/zaac.19966220502.

(11)    Xie, Y.; Wang, S.; Zhao, X. Phase Diagram and Structure of $CsSm_{(1-x)}Yb_xI_3$ Systems. *J. Alloys Compd* **1996**, *241* (1), 40–43. https://doi.org/10.1016/0925-8388(96)02196-2.

(12)    Meyer, G.; Gerlitzki, N.; Hammerich, S. Rare-Earth Diiodides and Derivatives. *J. Alloys Compd* **2004**, *380* (1), 71–78. https://doi.org/10.1016/j.jallcom.2004.03.031.

(13)    Wei, H.; Zhuravleva, M.; Yang, K.; Blalock, B.; Melcher, C. L. Effect of Ba Substitution in $CsSrI_3$:$Eu^{2+}$. *J. Cryst. Growth* **2013**, *384*, 27–32. https://doi.org/10.1016/j.jcrysgro.2013.09.007.

(14)    Wu, Y.; Gokhale, S. S.; Lindsey, A. C.; Zhuravleva, M.; Stand, L.; Johnson, J. A. I.; Loyd, M.; Koschan, M.; Melcher, C. L. Toward High Energy Resolution in $CsSrI_3$/$Eu^{2+}$ Scintillating Crystals: Effects of Off-Stoichiometry and $Eu^{2+}$ Concentration. *Cryst. Growth Des.* **2016**, *16* (12), 7186–7193. https://doi.org/10.1021/acs.cgd.6b01375.

(15)    Zhang, Y.; Deng, Z.; Li, K.; Ye, Y.; Liu, C. $Eu^{2+}$:$CsCaX_3$ (X = Cl, Br, I) Perovskite Nanocrystals in Glasses for Blue Light-Emitting Applications. *J. Mater. Chem. C* **2023**, *11* (30), 10389–10397. https://doi.org/10.1039/D3TC01704D.

(16)   Goldschmidt, V. M. Die Gesetze der Krystallochemie. *Naturwissenschaften* **1926**, *14* (21), 477–485. https://doi.org/10.1007/BF01507527.

(17)   Kieslich, G.; Sun, S.; Cheetham, A. K. Solid-State Principles Applied to Organic–Inorganic Perovskites: New Tricks for an Old Dog. *Chem. Sci.* **2014**, *5* (12), 4712–4715. https://doi.org/10.1039/C4SC02211D.

(18)   Kieslich, G.; Sun, S.; Cheetham, A. K. An Extended Tolerance Factor Approach for Organic–Inorganic Perovskites. *Chem. Sci.* **2015**, *6* (6), 3430–3433. https://doi.org/10.1039/C5SC00961H.

(19)   Sun, Q.; Yin, W.-J. Thermodynamic Stability Trend of Cubic Perovskites. *J. Am. Chem. Soc.* **2017**, *139* (42), 14905–14908. https://doi.org/10.1021/jacs.7b09379.

(20)   Maughan, A. E.; Ganose, A. M.; Almaker, M. A.; Scanlon, D. O.; Neilson, J. R. Tolerance Factor and Cooperative Tilting Effects in Vacancy-Ordered Double Perovskite Halides. *Chem. Mater.* **2018**, *30* (11), 3909–3919. https://doi.org/10.1021/acs.chemmater.8b01549.

(21)   Vishnoi, P.; Seshadri, R.; Cheetham, A. K. Why Are Double Perovskite Iodides so Rare? *J. Phys. Chem. C* **2021**, *125* (21), 11756–11764. https://doi.org/10.1021/acs.jpcc.1c02870.

(22)   Kent, G. T.; Morgan, E.; Albanese, K. R.; Kallistova, A.; Brumberg, A.; Kautzsch, L.; Wu, G.; Vishnoi, P.; Seshadri, R.; Cheetham, A. K. Elusive Double Perovskite Iodides: Structural, Optical, and Magnetic Properties. *Angew. Chem., Int. Ed. Engl.* **2023**, *62* (32), e202306000. https://doi.org/10.1002/anie.202306000.

(23)   Kluherz, K. T.; Mergelsberg, S. T.; De Yoreo, J. J.; Gamelin, D. R. Structure and Stability of the Iodide Elpasolite, $Cs_2AgBiI_6$. *Chem. Mater.* **2023**, *35* (14), 5699–5708. https://doi.org/10.1021/acs.chemmater.3c01511.

(24)   Shannon, R. D. Revised Effective Ionic Radii and Systematic Studies of Interatomic Distances in Halides and Chalcogenides. *Acta Cryst A* **1976**, *32* (5), 751–767. https://doi.org/10.1107/S0567739476001551.

(25)   Sidey, V. On the Effective Ionic Radii for the Tin(II) Cation. *J. Phys. Chem. Solids* **2022**, *171*, 110992. https://doi.org/10.1016/j.jpcs.2022.110992.

(26)   Mitzi, D. B.; Liang, K. Preparation and Properties of $(C_4H_9NH_3)_2EuI_4$: A Luminescent Organic−Inorganic Perovskite with a Divalent Rare-Earth Metal Halide Framework. *Chem. Mater.* **1997**, *9* (12), 2990–2995. https://doi.org/10.1021/cm970352d.

(27)   Zhao, X.; Fu, P.; Li, P.; Du, H.; Zhu, J.; Ge, C.; Yang, L.; Song, B.; Wu, H.; Jin, T.; Guo, Q.; Wang, L.; Li, J.; Xiao, Z.; Chang, J.; Niu, G.; Luo, J.; Tang, J. Solution-Processed Hybrid Europium (II) Iodide Scintillator for Sensitive X-Ray Detection. *Research* **2023**, *6*, 0125. https://doi.org/10.34133/research.0125.

(28)   Fabini, D. H.; Stoumpos, C. C.; Laurita, G.; Kaltzoglou, A.; Kontos, A. G.; Falaras, P.; Kanatzidis, M. G.; Seshadri, R. Reentrant Structural and Optical Properties and Large Positive Thermal Expansion in Perovskite Formamidinium Lead Iodide. *Angew. Chem. Int. Ed* **2016**, *55* (49), 15392–15396. https://doi.org/10.1002/anie.201609538.

(29)   Yamada, Y.; Yamada, T.; Phuong, L. Q.; Maruyama, N.; Nishimura, H.; Wakamiya, A.; Murata, Y.; Kanemitsu, Y. Dynamic Optical Properties of $CH_3NH_3PbI_3$ Single Crystals As Revealed by One- and Two-Photon Excited Photoluminescence Measurements. *J. Am. Chem. Soc.* **2015**, *137* (33), 10456–10459. https://doi.org/10.1021/jacs.5b04503.

(30)   Travis, W.; Glover, E. N. K.; Bronstein, H.; Scanlon, D. O.; Palgrave, R. G. On the Application of the Tolerance Factor to Inorganic and Hybrid Halide Perovskites: A Revised System. *Chem. Sci.* **2016**, *7* (7), 4548–4556. https://doi.org/10.1039/C5SC04845A.

(31)   Weber, O. J.; Ghosh, D.; Gaines, S.; Henry, P. F.; Walker, A. B.; Islam, M. S.; Weller, M. T. Phase Behavior and Polymorphism of Formamidinium Lead Iodide. *Chem. Mater.* **2018**, *30* (11), 3768–3778. https://doi.org/10.1021/acs.chemmater.8b00862.

(32)   Onoda-Yamamuro, N.; Yamamuro, O.; Matsuo, T.; Suga, H. P-T Phase Relations of $CH_3NH_3PbX_3$ (X = Cl, Br, I) Crystals. *J. Phys. Chem. Solids* **1992**, *53* (2), 277–281. https://doi.org/10.1016/0022-3697(92)90056-J.

(33)   Yu, X.; Qin, Y.; Peng, Q. Probe Decomposition of Methylammonium Lead Iodide Perovskite in $N_2$ and $O_2$ by in Situ Infrared Spectroscopy. *J. Phys. Chem. A* **2017**, *121* (6), 1169–1174. https://doi.org/10.1021/acs.jpca.6b12170.

(34)   Murugadoss, G.; Thangamuthu, R.; Rajesh Kumar, M. Formamidinium Lead Iodide Perovskite: Structure, Shape and Optical Tuning via Hydrothermal Method. *Mater. Lett.* **2018**, *231*, 16–19. https://doi.org/10.1016/j.matlet.2018.08.003.

(35)   Uwamino, Y.; Ishizuka, T.; Yamatera, H. X-Ray Photoelectron Spectroscopy of Rare-Earth Compounds. *J. Electron Spectrosc. Relat. Phenom.* **1984**, *34* (1), 67–78. https://doi.org/10.1016/0368-2048(84)80060-2.

(36)   Axe, J. D.; Sorokin, P. P. Divalent Rare Earth Spectra Selection Rules and Spectroscopy of $SrCl_2$: $Sm^{2+}$. *Phys. Rev.* **1963**, *130* (3), 945–952. https://doi.org/10.1103/PhysRev.130.945.

(37)   Wang, S.-H. $SmI_2$: A MOST USEFUL MATERIAL. *Rev. Inorg. Chem.* **1990**, *11* (1), 1–20. https://doi.org/10.1515/RE-VIC.1990.11.1.1.

(38)   Prasad, E.; Knettle, B. W.; Flowers II, R. A. Photoinduced Electron Transfer Reactions by $SmI_2$ in THF: Luminescence Quenching Studies and Mechanistic Investigations. *Chem. Eur. J* **2005**, *11* (10), 3105–3112. https://doi.org/10.1002/chem.200401163.

(39)   Schäfer, T. C.; Sorg, J. R.; Sedykh, A. E.; Müller-Buschbaum, K. Red Emitting Sm(II) Phosphors: Thermally Switchable Luminescence in $Sm(AlX_4)_2$ (X = Cl, Br) by 5d–4f and Intra-4f Transitions. *Chem. Commun.* **2021**, *57* (90), 11984–11987. https://doi.org/10.1039/D1CC05357D.

(40)   Dorenbos, P. Anomalous Luminescence of $Eu^{2+}$ and $Yb^{2+}$ in Inorganic Compounds. *J. Phys.: Condens. Matter* **2003**, *15* (17), 2645. https://doi.org/10.1088/0953-8984/15/17/318.

(41)   Alekhin, M. S.; Awater, R. H. P.; Biner, D. A.; Krämer, K. W.; de Haas, J. T. M.; Dorenbos, P. Luminescence and Spectroscopic Properties of $Sm^{2+}$ and $Er^{3+}$ Doped $SrI_2$. *J. Lumin.* **2015**, *167*, 347–351. https://doi.org/10.1016/j.jlumin.2015.07.002.

(42)   Loef, E. V. D. van; Dorenbos, P.; Eijk, C. W. E. van; Krämer, K. W.; Güdel, H. U. Scintillation Properties of $K_2LaX_5$:$Ce^{3+}$ (X=Cl, Br, I). *Nucl. Instrum. Methods Phys. Res.* **2005**, *537* (1), 232–236. https://doi.org/10.1016/j.nima.2004.08.016.

(43)   Awater, R. H. P.; Alekhin, M. S.; Biner, D. A.; Krämer, K. W.; Dorenbos, P. Converting $SrI_2$:$Eu^{2+}$ into a near Infrared Scintillator by $Sm^{2+}$ Co-Doping. *J. Lumin.* **2019**, *212*, 1–4. https://doi.org/10.1016/j.jlumin.2019.04.002.

(44)   Xinhua, Z.; Shihua, W.; Baopeng, C. Fluorescence Spectra of $ARE_2I_5$ and $AREI_3$ in the Solid State (A = K, Rb, Cs, Ti; RE = Sm, Eu). *J. Alloys Compd* **1992**, *180* (1), 235–238. https://doi.org/10.1016/0925-8388(92)90386-N.

(45)   Yang, K.; Zhuravleva, M.; Melcher, C. L. Crystal Growth and Characterization of $CsSr_{1−x}Eu_xI_3$ High Light Yield Scintillators. *Phys. Status Solidi RRL* **2011**, *5* (1), 43–45. https://doi.org/10.1002/pssr.201004434.

(46)   Lebedynskiy, A. M.; Shiran, N. V.; Gektin, A. V.; Fedorov, A. G.; Vasyukov, S. A.; Mateychenko, P. V. Structure and Luminescence of CsI:Eu Columnar Films. *J Appl Spectrosc* **2012**, *79* (4), 583–588. https://doi.org/10.1007/s10812-012-9643-x.

(47)   Dieke, G. H.; Sarup, R. Fluorescence Spectrum and the Energy Levels of the $Sm^{2+}$ Ion. *J. Chem. Phys* **2004**, *36* (2), 371–377. https://doi.org/10.1063/1.1732512.

(48)   Huang, K.; Zhu, B. *Selected Papers of Kun Huang: With Commentary*; World Scientific, 2000; Vol. 23.

(49)   Bhoyar, P. D.; Nair, G. B.; Dhoble, S. J. Photoluminescence Properties of Different Luminescent Ions ($Ce^{3+}$, $Eu^{3+}$, $Eu^{2+}$, $Dy^{3+}$, $Cu^+$) in $K_2LaCl_5$ Host Matrix. *Optik* **2017**, *134*, 33–44. https://doi.org/10.1016/j.ijleo.2017.01.024.

(50)   Lyu, K.; Song, E.; Xia, Z. $Eu^{2+}$ Doped Halide Perovskite $KCaCl_3$ with High-Efficiency Blue Emission and Scintillation Application. *J. Mater. Chem. C* **2022**, *10* (25), 9636–9643. https://doi.org/10.1039/D2TC01117D.

(51)   Meyer, G. Halo-Elpasolites, VI [1] The First Iodo-Elpasolites, $Cs_2B_IM_{III}I_6$ ( $B^I$ = Li , Na). *Z. Naturforsch. B* **1980**, *35* (3), 394–396. https://doi.org/doi:10.1515/znb-1980-0327.

(52)   Metallinou, M. M.; Nalbandian, L.; Papatheodorou, G. N.; Voigt, W.; Emons, H. H. Thermal Analysis and Raman Spectroscopic Measurements on the Scandium Iodide-Cesium Iodide System. *Inorg.*

*Chem.* **1991**, *30* (22), 4260–4264. https://doi.org/10.1021/ic00022a030.

(53) Dorenbos, P. Energy of the First 4f$_7$→4f$_6$5d Transition of Eu$^{2+}$ in Inorganic Compounds. *J. Lumin.* **2003**, *104* (4), 239–260. https://doi.org/10.1016/S0022-2313(03)00078-4.

(54) Liu, Y.; Lu, H.; Niu, J.; Zhang, H.; Lou, S.; Gao, C.; Zhan, Y.; Zhang, X.; Jin, Q.; Zheng, L. Temperature-Dependent Photoluminescence Spectra and Decay Dynamics of MAPbBr$_3$ and MAPbI$_3$ Thin Films. *AIP Advances* **2018**, *8* (9), 095108. https://doi.org/10.1063/1.5042489.

(55) Alekhin, M. S.; Biner, D. A.; Krämer, K. W.; Dorenbos, P. Optical and Scintillation Properties of CsBa$_2$I$_5$:Eu$^{2+}$. *J. Lumin.* **2014**, *145*, 723–728. https://doi.org/10.1016/j.jlumin.2013.08.058.

(56) Suta, M.; Wickleder, C. Photoluminescence of CsMI$_3$:Eu$^{2+}$ (M = Mg, Ca, and Sr) – a Spectroscopic Probe on Structural Distortions. *J. Mater. Chem. C* **2015**, *3* (20), 5233–5245. https://doi.org/10.1039/C5TC00515A.

(57) Mugiraneza, S.; Hallas, A. M. Tutorial: A Beginner's Guide to Interpreting Magnetic Susceptibility Data with the Curie-Weiss Law. *Commun Phys* **2022**, *5* (1), 95. https://doi.org/10.1038/s42005-022-00853-y.

(58) Carlin, R. L. *Magnetochemistry*; Springer Science & Business Media, 1986.

(59) Suematsu, H.; Ohmatsu, K.; Sakakibara, T.; Date, M.; Suzuki, M. Magnetic Properties of Europium-Graphite Intercalation Compound C$_6$Eu. *Synth. Met.* **1983**, *8* (1), 23–30. https://doi.org/10.1016/0379-6779(83)90005-X.

(60) Guillou, F.; Paudyal, D.; Mudryk, Y.; Pathak, A. K.; Smetana, V.; Mudring, A.-V.; Pecharsky, V. K. Metamagnetic Transition, Magnetocaloric Effect and Electronic Structure of the Rare-Earth Anti-Perovskite SnOEu$_3$. *J. Magn. Magn. Mater.* **2020**, *501*, 166405. https://doi.org/10.1016/j.jmmm.2020.166405.

(61) G F Goya; R C Mercader; M T Causa; M Tovar. Magnetic Properties of Pnma-R$_2$BAZnO$_5$ Oxides (R = Sm, Eu, Dy and Ho). *J. Phys. Condens. Matter* **1996**, *8* (44), 8607. https://doi.org/10.1088/0953-8984/8/44/012.

(62) Van Vleck, J. H. *Electric and Magnetic Susceptibilities*; Clarendon Press, 1932.

(63) Holmes, L.; Sherwood, R.; Van Uitert, L. G.; Hüfner, S. Paramagnetic Anisotropy and Crystal-Field Splittings in EuAlO$_3$. *Phys. Rev.* **1969**, *178* (2), 576–579. https://doi.org/10.1103/PhysRev.178.576.

(64) Ishii, Y.; Chen, J.; Yoshida, H. K.; Oda, M.; Christianson, A. D.; Yamaura, K. High-Pressure Synthesis, Crystal Structure, and Magnetic Properties of the Shastry-Sutherland-Lattice Oxides BaLn$_2$ZnO$_5$ (Ln = Pr, Sm, Eu). *J. Solid State Chem.* **2020**, *289*, 121489. https://doi.org/10.1016/j.jssc.2020.121489.

(65) Orbach, R.; Pincus, P. Phonon-Induced Corrections to the Van Vleck Temperature-Independent Susceptibility. *Phys. Rev.* **1966**, *143* (1), 168–171. https://doi.org/10.1103/PhysRev.143.168.

(66) George, N. C.; Denault, K. A.; Seshadri, R. Phosphors for Solid-State White Lighting. *Annu. Rev. Mater. Res.* **2013**, *43* (1), 481–501. https://doi.org/10.1146/annurev-matsci-073012-125702.

(67) Laurita, G.; Seshadri, R. Chemistry, Structure, and Function of Lone Pairs in Extended Solids. *Acc. Chem. Res.* **2022**, *55* (7), 1004–1014. https://doi.org/10.1021/acs.accounts.1c00741.

(68) Fabini, D. H.; Seshadri, R.; Kanatzidis, M. G. The Underappreciated Lone Pair in Halide Perovskites Underpins Their Unusual Properties. *MRS Bulletin* **2020**, *45* (6), 467–477. https://doi.org/10.1557/mrs.2020.142.
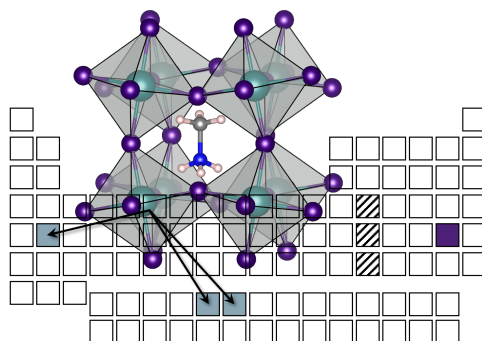
Synopsis: 3D hybrid perovskite iodides are synthesized using the alkaline earth and divalent lanthanide metals; their structural, optical, magnetic, and photoluminescence properties are recorded and discussed.

# Supporting information for:

## Hybrid Iodide Perovskites of Divalent Alkaline Earth and Lanthanide Elements

Greggory T. Kent[a], Jiale Zhuang[a], Kaitlin R. Albanese[a][b], Arava Zohar[a], Emily Morgan[a], Anna Kallistova[a], Linus Kautzsch[a], Alexander A. Mikhailovsky[b], Pratap Vishnoi[c], Ram Seshadri*[a][b], and Anthony K. Cheetham*[a][d]

[a]     Materials Department and Materials Research Laboratory, University of California, Santa Barbara, CA 93106 (USA)

[b]     Department of Chemistry and Biochemistry, University of California, Santa Barbara, CA 93106 (USA)

[c]      New Chemistry Unit and International Centre for Materials Science, Jawaharlal Nehru Centre for Advanced Scientific Research (JNCASR), Bangalore 560064 (India)

[d]     Department of Materials Science & Engineering, National University of Singapore, 117576 Singapore (Singapore)

*To whom correspondence should be addressed. Email: seshadri@mrl.ucsb.edu and akc30@cam.ac.uk

**Table of Contents**

**Experimental**

**General.** All reactions and subsequent manipulations were performed under strictly anaerobic and anhydrous conditions under an atmosphere of argon. All reagents were purchased from commercial vendors as anhydrous salts and used as received.

**Powder X-ray diffraction measurements.** Laboratory XRD patterns of all compounds were collected using a home-built air free sample holder with a beryllium window, to prevent sample decomposition. The Be window did show a systematic effect on peak intensities and shape at lower angles, which could not be corrected for. The powder XRD data were analyzed using the TOPAS software suite.[1] Initial Pawley refinements were performed to determine lattice parameters and peak shapes.[2] Subsequently, Rietveld refinements were performed to determine background, zero-point error, and atomic positions. All refinements excluded a region between 49.0 and 53.5 Cu-2θ to avoid errors associated with refining the both the sample and signal from the Be window.

**Magnetic measurements.** The magnetic properties of all compounds were recorded using a Quantum Design Magnetic Property Measurement System SQUID vibrating sample magnetometer (MPMS3 SQUID-VSM). All powdered samples were loaded in plastic caps under an argon atmosphere and mounted on a brass holder for measurements. Zero-field cooled and field cooled measurements were taken on warming between $T = 1.8$ K and 300 K under a constant field of 0.5 Tesla.

**Optical properties.** Diffuse reflectance spectra were collected on a Shimadzu UV-3600 UV–vis–NIR spectrometer using $BaSO_4$ (Sigma Aldrich) as the reference for 100% reflectance. The spectra were collected by adding powdered samples, diluted with $BaSO_4$, to a sample holder and applying transparent tape over the samples to prevent decomposition from air. The diffuse reflectance data were transformed into the absorbance by using the Kubelka–Munk (K-M) expression. Steady-state photoluminescence data were obtained using a Jobin-Yvon HORIBA FluoroMax-4 (xenon source, 1 nm step size) equipped with a solid-state sample holder. Photoluminescence spectra for $AEuI_3$ ($A$ = Ma, Fa) were also collected by adding powdered samples, diluted with $BaSO_4$, to a sample holder and applying transparent tape over the samples to prevent decomposition from air. Photoluminescence data were analyzed using the FluorEssence (v3.5) software powered by Origin. Photoluminescence data for $MASmI_3$ could not be collected to a low enough wavelength using the above set-up and all photoluminescence collected on this composition was done using the set-up below.

The temperature-dependent steady state photoluminescence (PL) measurements were performed on a home-built fluorometer setup. The PL was excited by a solid state laser beam (Coherent OBIS) with 375 nm wavelength at 45 degrees angle of incidence. The incident beam power was <500 uW focused into the spot with a Gaussian diameter of ~100um. The PL was collected in 90 degrees geometry with an optical lens system and focused on the input slit of a spectrometer (Acton SP-500) equipped with a charge-coupled device (CCD) camera (Princeton Instruments PIXIS:400) which can detect light in the range 300-1050 nm. The CCD detector was protected from the excitation light by a long-pass interference filter (Omega Filters ALP400). The spectrum, collected by the CCD camera, was corrected for the instrument response by measuring the spectrum of a black body-like light source (Ocean Optics HL-1) and calculating the appropriate correction factor. To control the temperature, the sample was placed into an LN2-cooled cryostat

(Janis VPF-100 with Thermaltake 323 controller). The spectra were processed and fit using the Fityk software package.

**Differential Scanning Calorimetry.** Differential Scanning Calorimetry (DSC) was performed using a TA Instruments DSC Q2000 at a heating/cooling rate of 10 °C/min using 3–5 mg of sample in a sealed aluminum pan.

**X-ray Photoelectron Spectroscopy.** X-ray photoelectron spectroscopy measurements were performed using a Thermo Fisher ESCALAB Xi$^+$ XPS system with a monochromated aluminum anode (1486.7 eV). Powder samples were pressed onto carbon tape and were transferred to the instrument using a homemade air-free sample holder. Since all measured samples were semiconducting, charge compensation was applied, and all spectra were referenced to the C 1s peak of carbon at 284.5 eV.

**Synthesis.** In a typical synthesis, stoichiometric quantities of MAI or FAI, $MI_2$ ($M$ = Sm, Eu, Sr) were weighed in an argon glovebox with oxygen and water levels of <0.5 ppm. These materials were ground and pressed into a pellet that was then loaded into an alumina crucible inside a silica tube. The reaction tube was sealed under vacuum and heated to 210 ºC. Reactions containing MAI were heated for 24 h, while reactions containing FAI required 72 h for complete conversion. After heating the reaction tubes were brought back into the glovebox, the pellet removed from the sealed tube and ground into fine powders for subsequent property measurements.

**Table S1.** TF and radius ratio of selected 3D perovskite compositions.

| Compound | $M^{II}$ radius | $TF$ | $\mu$ |
|---|---|---|---|
| $CsCaI_3$ | 1.0 | 0.9017 | 0.45455 |
| $MACaI_3$ | 1.0 | 0.96579 | 0.45455 |
| $FACaI_3$ | 1.0 | 1.04535 | 0.45455 |
| $CsSrI_3$ | 1.18 | 0.85368 | 0.53636 |
| $MASrI_3$ | 1.18 | 0.91436 | 0.53636 |
| $FASrI_3$ | 1.18 | 0.98968 | 0.53636 |
| $CsBaI_3$ | 1.35 | 0.8128 | 0.61364 |
| $MABaI_3$ | 1.35 | 0.87057 | 0.61364 |
| $FABaI_3$ | 1.35 | 0.94229 | 0.61364 |
| $CsEuI_3$ | 1.17 | 0.85621 | 0.53182 |
| $MAEuI_3$ | 1.17 | 0.91707 | 0.53182 |
| $FAEuI_3$ | 1.17 | 0.99262 | 0.53182 |
| $CsSmI_3$ | 1.18 | 0.85368 | 0.53636 |
| $MASmI_3$ | 1.18 | 0.91436 | 0.53636 |
| $FASmI_3$ | 1.18 | 0.98968 | 0.53636 |
| $CsYbI_3$ | 1.02 | 0.8961 | 0.46364 |
| $MAYbI_3$ | 1.02 | 0.95979 | 0.46364 |
| $FAYbI_3$ | 1.02 | 1.03886 | 0.46364 |
| $CsPbI_3$ | 1.19 | 0.85116 | 0.54091 |
| $MAPbI_3$ | 1.19 | 0.91166 | 0.54091 |
| $FAPbI_3$ | 1.19 | 0.98676 | 0.54091 |
| $CsSnI_3$ | 1.0 | 0.9017 | 0.45455 |
| $MASnI_3$ | 1.0 | 0.96579 | 0.45455 |
| $FASnI_3$ | 1.0 | 1.04535 | 0.45455 |

(Eq S1):

$$TF_P = \frac{r_A + r_X}{\sqrt{2}(M^{II} + r_X)}$$

(Eq S2):

$$\mu = \frac{r_M}{r_X}$$

**Table S2.** Table of crystallographic details for $AM^{II}I_3$ ($A$ = MA, $M^{II}$ = Sr, Sm, Eu; $A$ = FA, $M^{II}$ = Sr, Eu).

| empirical formula | MASrI$_3$ | MASmI$_3$ | MAEuI$_3$ | FASrI$_3$ | FAEuI$_3$ |
|---|---|---|---|---|---|
| crystal system | Tetragonal | Tetragonal | Tetragonal | Tetragonal | Tetragonal |
| space group | *I4/mcm* | *I4/mcm* | *I4/mcm* | *P4/mbm* | *P4/mbm* |
| vol (Å$^3$) | 1034.44(7) | 1030.7(1) | 1023.89(6) | 533.21(6) | 527.89(3) |
| a (Å) | 8.9449(3) | 8.9372(5) | 8.9191(2) | 9.1018(5) | 9.0716(2) |
| b (Å) | 8.9449(3) | 8.9372(5) | 8.9191(2) | 9.1018(5) | 9.0716(2) |
| c (Å) | 12.9288(3) | 12.9046(8) | 12.8709(4) | 6.4365(3) | 6.4146(2) |
| α (deg) | 90 | 90 | 90 | 90 | 90 |
| β (deg) | 90 | 90 | 90 | 90 | 90 |
| γ (deg) | 90 | 90 | 90 | 90 | 90 |
| R$_{wp}$ | 5.55% | 4.72% | 4.86% | 7.17% | 5.72% |
| R$_p$ | 4.04% | 3.38% | 3.29% | 5.04% | 3.66% |

**Table S3.** Atom positions for $MAM^{II}I_3$ ($M^{II}$ = Sr, Sm, Eu).

| Atom/Moiety | X | Y | Z | Wyckoff site |
|---|---|---|---|---|
| A | 0.5 | 0 | 0.5 | 4d |
| $M^{II}$ | 0 | 0 | 0 | 4c |
| I1 | 0 | 0 | 0.25 | 4a |
| I2 | Y+0.5 | Sr: 0.2036(2); Sm: 0.2029(3); Eu: 0.2040(2) | 0.5 | 8h |

**Table S4.** Atom positions for $FAM^{II}I_3$ ($M^{II}$ = Sr, Eu).

| Atom/Moiety | X | Y | Z | Wyckoff site |
|---|---|---|---|---|
| A | 0 | 0.5 | 0 | 2d |
| $M^{II}$ | 0 | 0 | 0.5 | 2b |
| I1 | 0 | 0 | 0 | 2a |
| I2 | Sr: 0.2854 (6); Eu:0.2818(5) | X+0.5 | 0.5 | 4h |
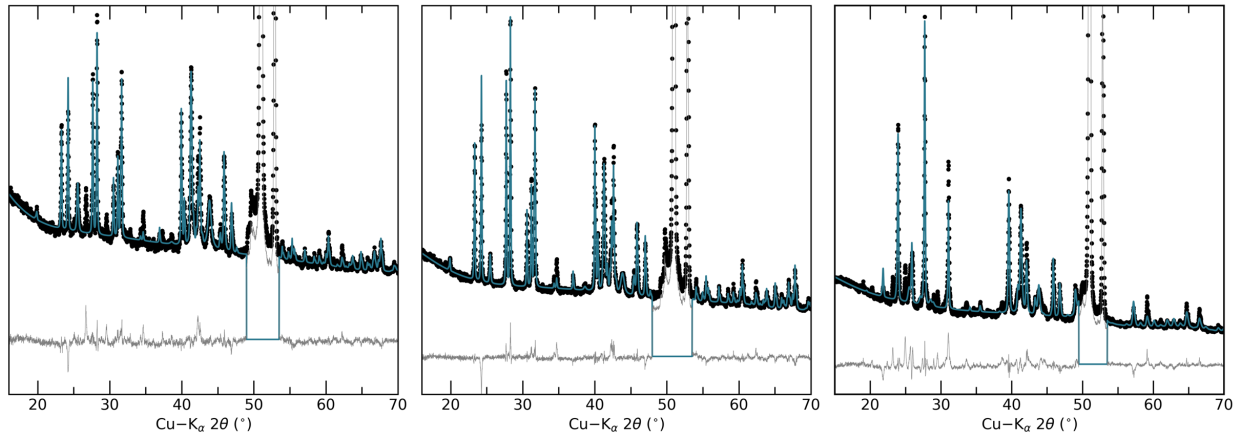


**Figure S1.** Powder XRD of MASmI$_3$ (left), MAEuI$_3$ (middle), and FASrI$_3$ (right) with Rietveld refinement (green line), difference (grey line), and respective structures, drawn to scale. For ease the region containing the major Be reflections has not been refined.
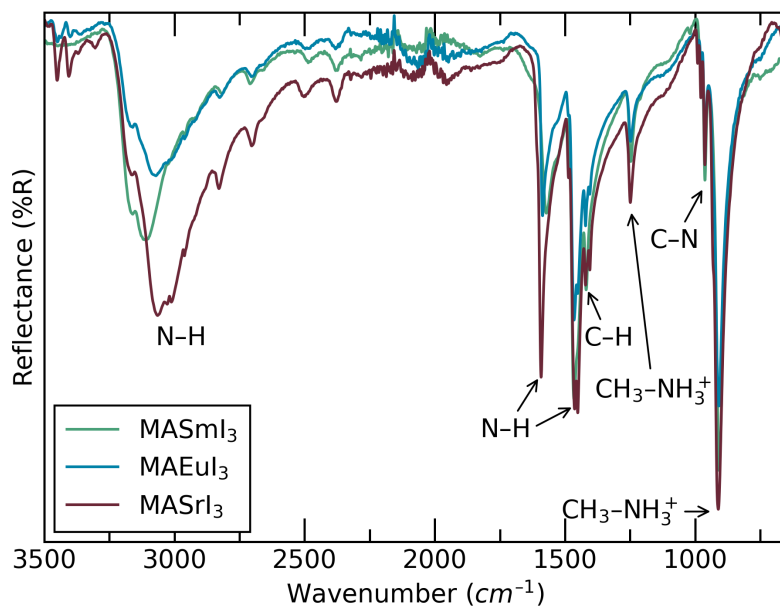
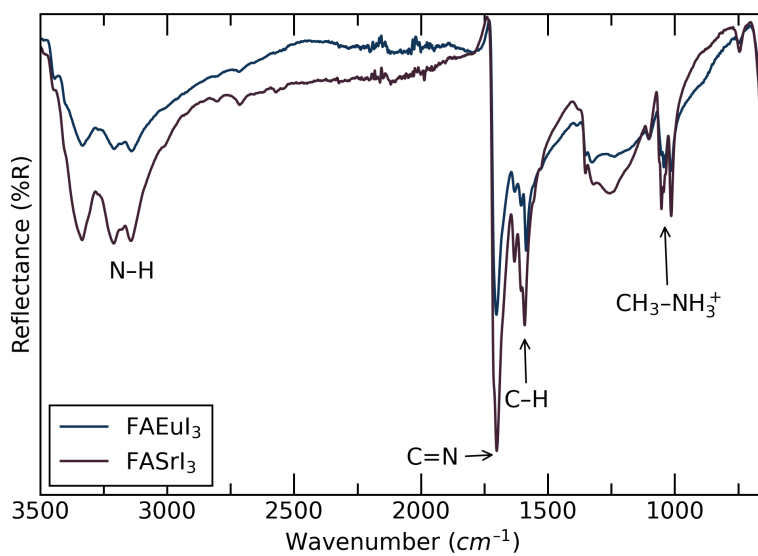**Figure S2.** ATR-IR spectrum of MA$B^{II}$I$_3$ ($B^{II}$ = Sm, Eu, Sr) with annotated absorbances.



**Figure S3.** ATR-IR spectrum of FA$B^{II}$I$_3$ ($B^{II}$ = Eu, Sr) with annotated absorbances.
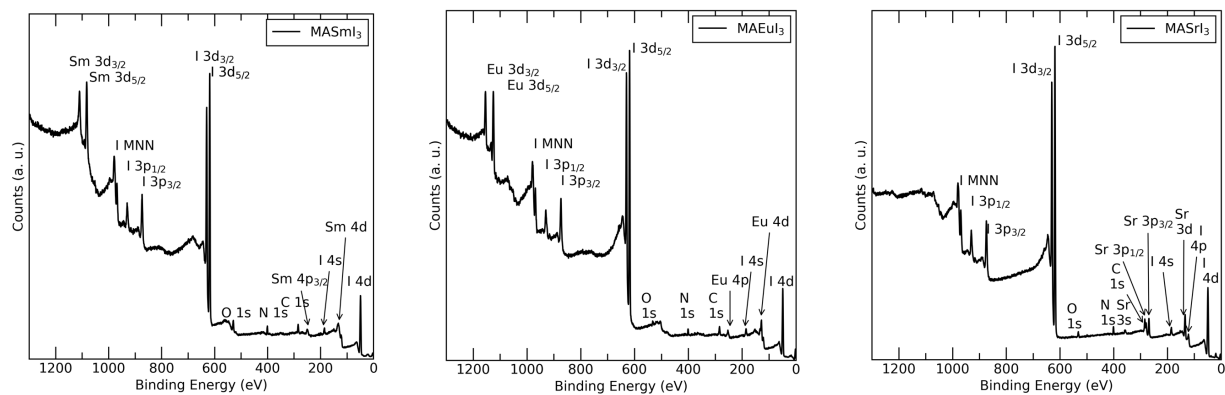
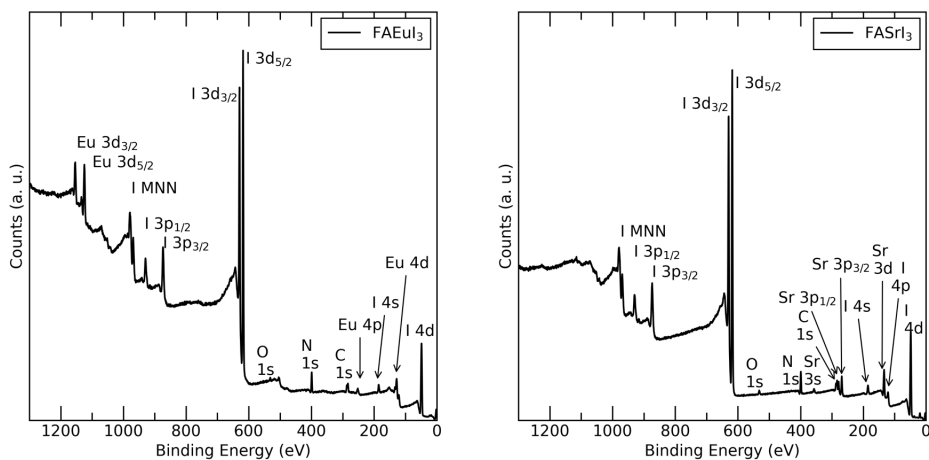**Figure S4.** Annotated XPS Spectra of $MAM^{II}I_3$ ($M^{II}$ = Sm, Eu, Sr).



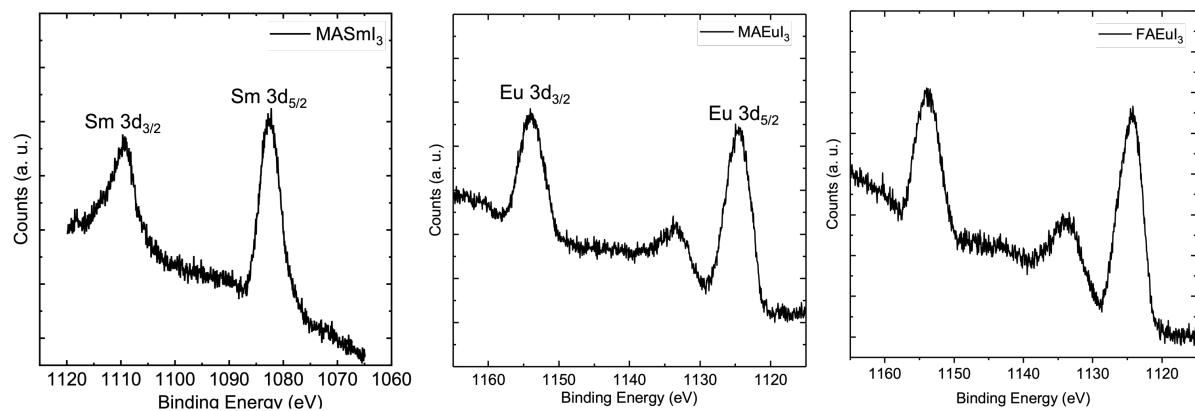**Figure S5.** Annotated XPS Spectra of $FAM^{II}I_3$ ($M^{II}$ = Eu, Sr).



**Figure S6**. High resolution 3d region XPS spectra for $MASmI_3$ (left), $MAEuI_3$ (center), $FAEuI_3$ (right).

**Table S5.** Selected binding energies (eV) obtained from XPS data.

| XPS Peaks | MASmI$_3$ | MAEuI$_3$ | MASrI$_3$ | FAEuI$_3$ | FASrI$_3$ |
|---|---|---|---|---|---|
| *Ln 3d$_{5/2}$* | 1082.6 | 1124.5 | - | 1124.3 | - |
| *Ln 3d$_{3/2}$* | 1109.3 | 1154.0 | - | 1153.8 | - |
| I *3p$_{3/2}$* | 873.5 | 873.8 | 874.0 | 873.6 | 873.5 |
| I *3p$_{1/2}$* | 930.1 | 929.6 | 930.4 | 929.7 | 930.0 |
| I *3d$_{5/2}$* | 618.1 | 618.5 | 618.5 | 618.0 | 618.0 |
| I *3d$_{3/2}$* | 629.6 | 630.0 | 630.5 | 629.5 | 629.5 |
| Sr *3p$_{3/2}$* | - | - | 268.5 | - | 268.7 |
| Sr *3p$_{1/2}$* | - | - | 279.1 | - | 278.6 |
| C *1s* | 286.2 | 286.5 | 286.4 | 286.9 | 287.0 |
| N *1s* | 400.5 | 401.0 | 400.6 | 399.0 | 399.0 |
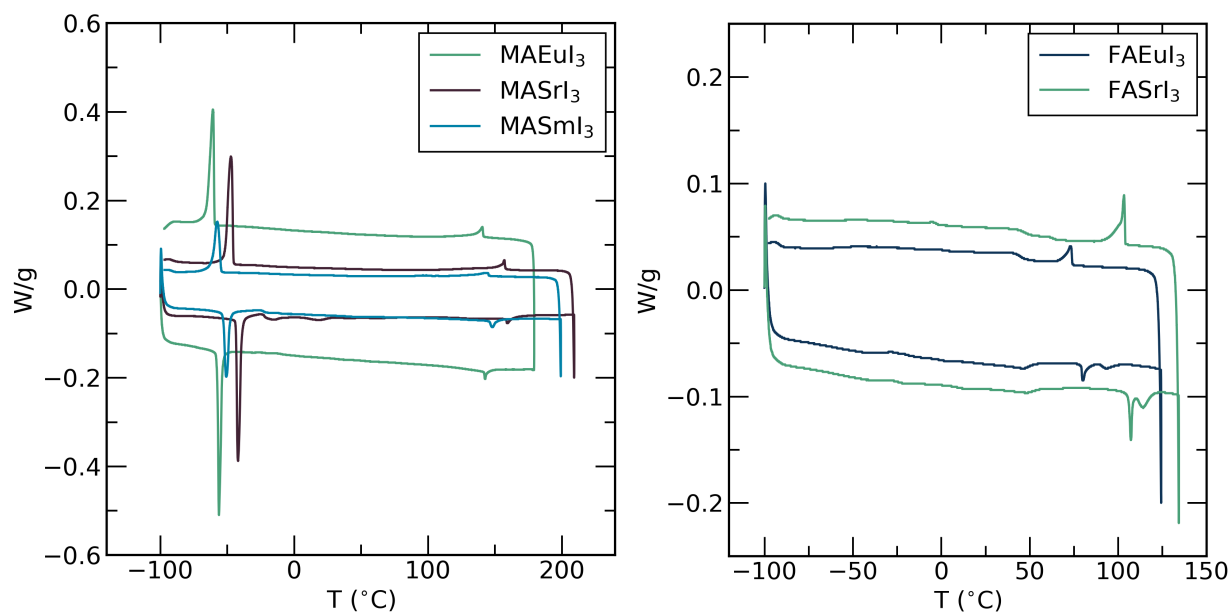


**Figure S7. DSC** thermograms of MA*M*$^{II}$I$_3$ (*M*$^{II}$ = Sm, Eu, Sr; Left) and FA*M*$^{II}$I$_3$ (*M*$^{II}$ = Eu, Sr; Right). The second heat and cool cycle, with a ramp rate of 10 °C min$^{-1}$.
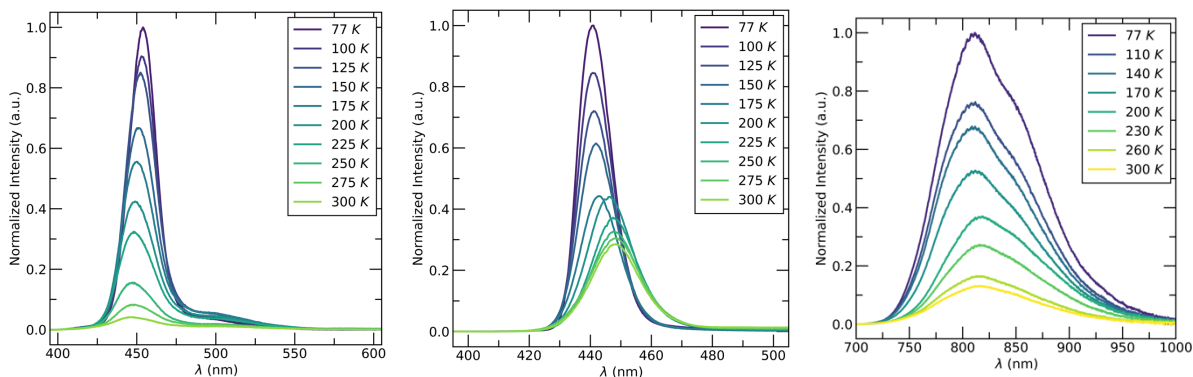
**Figure S8.** Variable temperature emission spectra of FAEuI₃ (left), MAEuI₃ (middle), and MASmI₃ (right), measured while exciting at 375 nm.
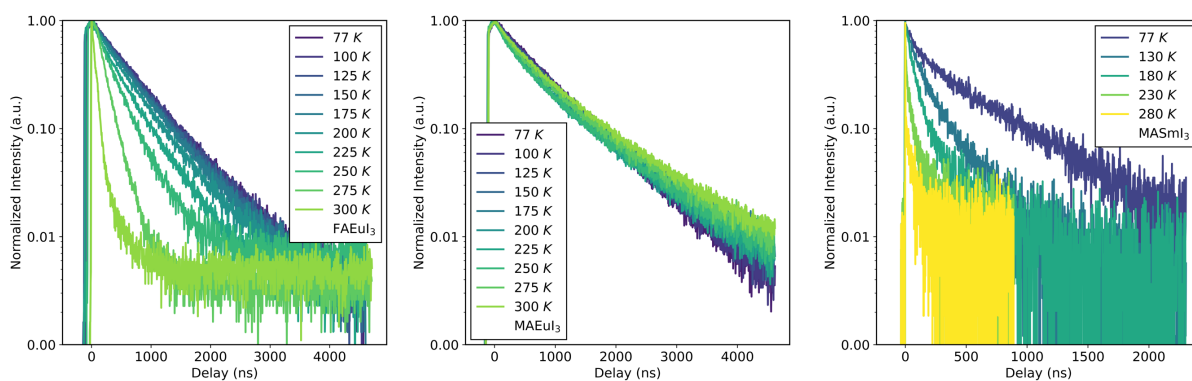


**Figure S9.** Variable temperature photoluminescence lifetime measurements of FAEuI₃ (left), MAEuI₃ (middle), and MASmI₃ (right), measured while exciting at 375 nm.
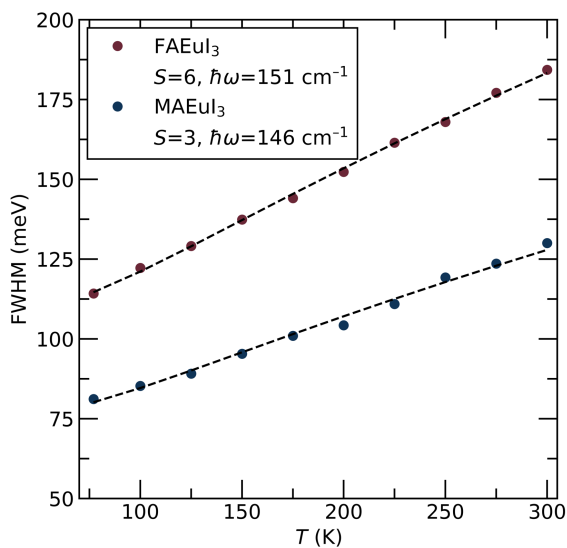


**Figure S10.** Temperature-dependent FWHM values for MAEuI₃ and FAEuI₃, fit using eq S3.

$$(\text{Eq. S3})^3 \quad \text{FWHM}(T) = 2.36\sqrt{S}\hbar\omega\sqrt{\coth\left(\frac{\hbar\omega}{2k_bT}\right)}$$

$$(\text{Eq. S4}) \quad \Delta E_S = (2S-1)\hbar\omega$$
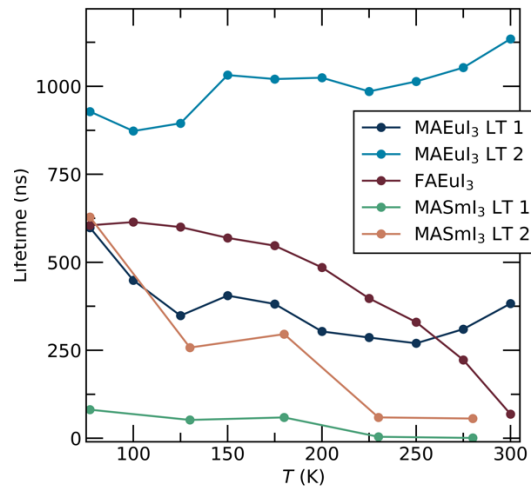
**Figure S11.** Variable temperature photoluminescence lifetimes for MAEuI$_3$, MASmI$_3$ (fit with double exponential, lifetimes 1 and 2) and for FAEuI$_3$ (fit with single exponential).
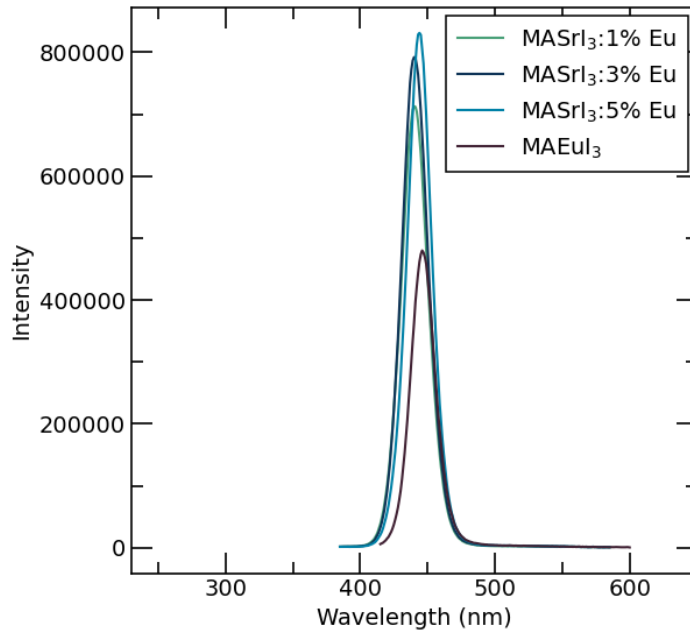
**Figure S12.** Photoluminescent response of MASr$_{1-x}$ Eu$_x$I$_3$ and respective band passes (x = 0.01 (0.9nm), 0.03 (0.9nm), 0.05 (0.9nm), 1.00 (2.1nm))
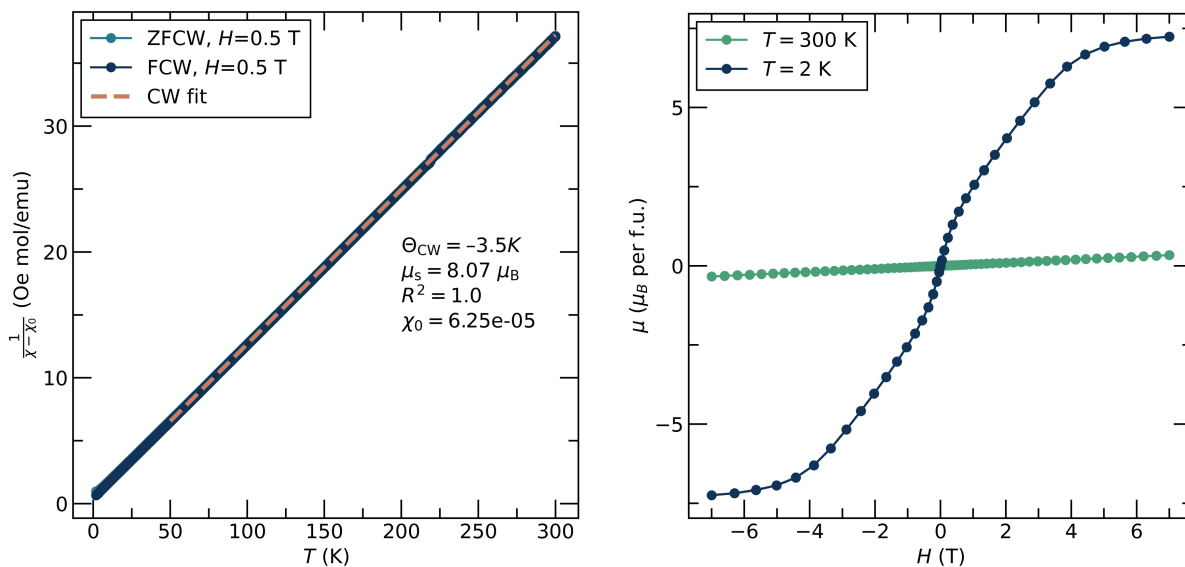
S10

**Figure S13.** Inverse magnetic susceptability vs temperature plot of MAEuI$_3$ ($\chi^{-1}$, left plot) with CW fit (dashed line) and M vs H curves of MAEuI$_3$ at 2 K and 300 K (right plot).
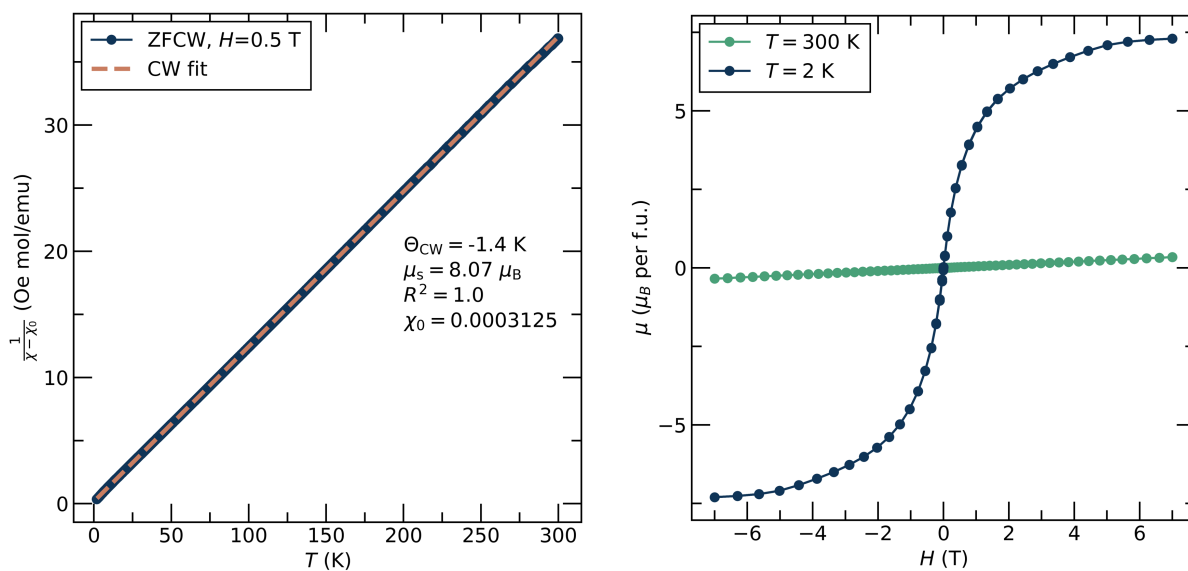


**Figure S14.** Inverse magnetic susceptability vs temperature plot of FAEuI$_3$ ($\chi^{-1}$, left plot) with CW fit (dashed line) and M vs H curves of FAEuI$_3$ at 2 K and 300 K (right plot).
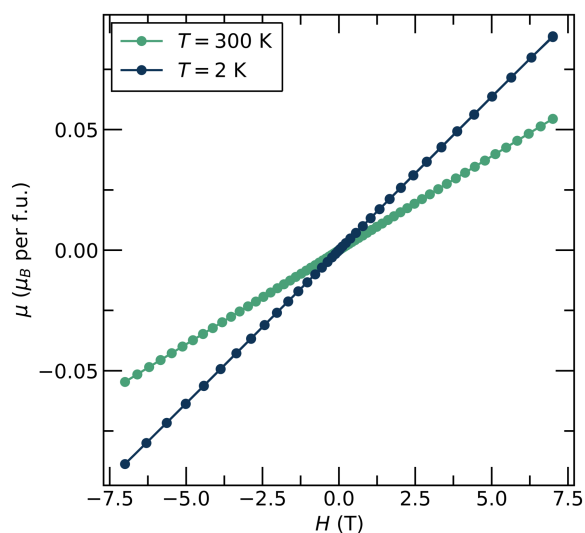
**Figure S15**. M vs H curves of MASmI$_3$ at 2 K and 300 K.

(Eq S5)[4]

$$\chi = \left(\frac{N\beta}{3kTx}\right) \times \frac{24 + \left(\frac{27x}{2} - \frac{3}{2}\right)e^{-x} + \left(\frac{135x}{2} - \frac{5}{2}\right)e^{-3x} + \left(\frac{189x}{2} - \frac{7}{2}\right)e^{-6x} + \left(\frac{405x}{2} - \frac{9}{2}\right)e^{-10x} + \left(\frac{1485x}{2} - \frac{11}{2}\right)e^{-15x} + \left(\frac{2457x}{2} - \frac{13}{2}\right)e^{-21x}}{1 + 3e^{-x} + 5e^{-3x} + 7e^{-6x} + 9e^{-10x} + 11e^{-15x} + 13e^{-21x}}$$
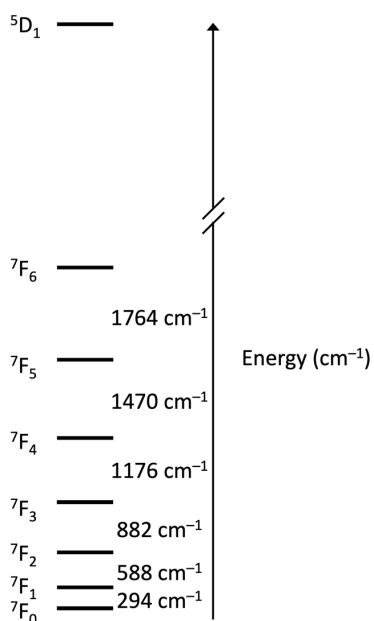
$$x = \frac{\zeta}{kT}$$



**Figure S16.** $^7F_x$ (x = 0–6) Multiplet Splittings for Sm(II) in MASmI$_3$ derived by fitting the experimental suceptibility data.

**References.**

(1) Coelho, A. A. TOPAS and TOPAS-Academic: An Optimization Program Integrating Computer Algebra and Crystallographic Objects Written in C++. *J. Appl. Cryst.* **2018**, *51* (1), 210–218. https://doi.org/10.1107/S1600576718000183.

(2) Pawley, G. S. Unit-Cell Refinement from Powder Diffraction Scans. *J Appl Cryst* **1981**, *14* (6), 357–361. https://doi.org/10.1107/S0021889881009618.

(3) Huang, K.; Zhu, B. *Selected Papers of Kun Huang: With Commentary*; World Scientific, 2000; Vol. 23.

(4) Van Vleck, J. H. *Electric and Magnetic Susceptibilities*; Clarendon Press, 1932.